I.J. Wireless and Microwave Technologies, **2025, 3, 19-36**
Published Online on June 8, 2025 by MECS Press (http://www.mecs-press.org/)
DOI: 10.5815/ijwmt.2025.03.02

3D mmWave MIMO Channel Modeling and Reconstruction for Street Canyon and High-rise Scenarios

Olabode Idowu-Bismark*
Department of Electrical and Information Engineering and Covenant Applied Informatics & Communication African Center of Excellence (CApIC-ACE), Covenant University, Ota, Nigeria
E-mail: idowubismarkolabode@gmail.com
ORCID iD: https://orcid.org/0000-0002-7958-1121
*Corresponding Author

Oluwadamilola Oshin
Department of Electrical and Information Engineering and Covenant Applied Informatics & Communication African Center of Excellence (CApIC-ACE), Covenant University, Ota, Nigeria
E-mail: damilola.adu@covenantuniversity.edu.ng
ORCID iD: https://orcid.org/0000-0001-9313-7441

Emmanuel Adetiba
Department of Electrical and Information Engineering and Covenant Applied Informatics & Communication African Center of Excellence (CApIC-ACE), Covenant University, Ota, Nigeria
HRA, Industrial Engineering Department, Durban University of Technology, Durban, South Africa
E-mail: emmanuel.adetiba@covenantuniversity.edu.ng
ORCID iD: https://orcid.org/0000-0001-9227-7389

Received: 27 June, 2023; Revised: 10 September, 2023; Accepted: 10 December, 2023; Published: 08 June, 2025

Abstract: The use of millimeter-wave (mmWave) and full-dimensional multiple-input multiple-output (FD-MIMO) antenna systems for 3D wireless communication is being exploited for enhanced network capacity improvement in the ongoing fifth-generation (5G) deployment. For adequate assessment of competing air interface, random access channelization, and beam alignment procedure in mmWave systems, adequate channel estimation and channel models for different use scenarios are necessary. Conventional pilot-based channel estimation methods are remarkably time-consuming as the number of users or antennas tends toward large numbers. Channel reconstruction has been identified as one of the solutions to the above problem. In this work, a ray-tracing study was conducted using a Wireless Insite ray tracing engine to predict measured statistics for large-scale channel parameters (LSPs). Other LSP such as the shadow fading (SF) were generated using algorithm 1. Algorithm 2 was used to generate the small-scale channel parameters (SSP). The LSPs and SSPs were used as input in algorithm 3 to generate the channel coefficients used for the channel reconstruction in the MATLAB LTE toolbox. The results provided an accurate reconstructed downlink channel state information (CSI) for FDD-based mmWave massive-MIMO system in both the line-of sight (LOS) and non-line of sight scenarios. The results provide an opportunity to adapt the transmitted signal to the CSI and thereby optimize the received signal for spatial multiplexing or to achieve low bit error rates in wireless communication.

Index Terms: 5G, mmWave Channel, Massive MIMO, 3D Channel Modeling, Channel Reconstruction

1. Introduction

The long-term evolution (LTE) infrastructure is under strain due to the explosively growing demand for mobile traffic brought on by everyone's need for an online presence on sites like Facebook, Twitter, YouTube, and video streaming [1,2]. LTE has developed into LTE-Advance, yet it is still unable to keep up with the demand for mobile data. The two aforementioned circumstances have made the 5G network necessary. It has been proposed in the literature that network densification (ND) is a method to meet the 5G requirements. For instance, the authors in [3] claimed that ND is a method to increase the capacity of a mobile network by 10 to 100 times. According to the study in [4], ND can provide 5G ultra-reliable low latency communication (URLLC) as well as 5G massive device connectivity, as claimed in [5]. Spatial densification and spectral aggregation are combined to form ND. In order to achieve spatial densification, small cells (Picocells, Femtocells) are placed over macrocell and massive multiple-input multiple-output (MIMO) technology is used for backhauling at the base station [6]. Large carrier frequencies are used in spectral aggregation, which range from 500 MHz to the mmWave (30 GHz-300 GHz) spectrum. Due to issues with space and wind loading, the antenna elements in massive MIMO are stacked in a planar array structure at the top of the base station (BS) and are known by the 3GPP as full-dimension MIMO (FD-MIMO) [7]. As seen in Figure 1, where FD-MIMO eNB with its many antennas allows the creation of different signal beams to be directed to users in the elevation domain while still having enough antennas to cater for users in the azimuth domain. Thus, FD-MIMO permits signal propagation in the three-dimensional (3D) domain unlike in the 2D domain offered by the current MIMO system. The use of FD-MIMO, a novel technique for improving system performance, uncovers brand-new issues that must be handled right away. These difficulties include creating precise 3D channel models, forecasting performance, doing analysis to account for the channel component's influence in the elevation domain, finding suitable deployment scenarios, etc. [8]. Other challenges include the acquisition of channel state information (CSI) at the base station (BS) for frequency division duplexing (FDD) systems. Knowledge of the channel state information (CSI) at a base station (BS) plays a significant role in attaining higher throughputs in 5G and beyond 5G cellular networks. For the BS to obtain the downlink CSI, the users need to feed back their downlink channel matrix which is estimated through downlink pilot training. In previous cellular networks leading up to the LTE-Advanced, base station antennas are limited to a maximum of eight for LTE-A with ample amount of network resources (time and frequency) available to form orthogonal pilots while the amount of feedback is relatively small. However, the combination of mmWave and MIMO system allows massive MIMO in 5G and future networks the use of hundreds, even thousands of antenna ports which however prevents the design of completely orthogonal pilot patterns since that induces a huge amount of overhead to the system and ultimately decreases the effectiveness of CSI utilization [9]

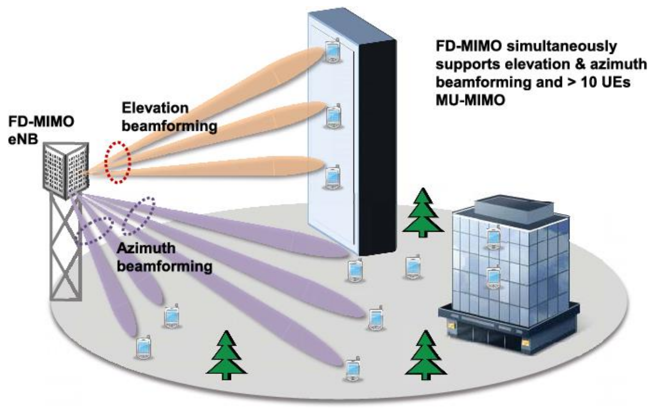

Fig. 1. Full Dimension MIMO enabling 3D-Beamforming [10]

The alternative is pilot reuse and the negative consequence of low accuracy of the CSI estimation which degrade the system [11] Thus, downlink CSI acquisition remains a key problem in FDD mmWave massive-MIMO systems and researchers have been probing for new solutions to obtain downlink CSI and design corresponding transmission schemes. Channel reconstruction has been identified as one of the solutions to the above problem. Also, for signal transmission studies, one needs a channel model that can simulate the spatial variation of mmWave channel impulse responses (CIRs) in treated operating environments [12] In such situation, suitable channel models are an indispensable prerequisite for candidate application scenarios. Such scenarios include the channel impulse response reconstruction for unmanned aerial vehicle (UAV) [13], and wearable [14]. Another area of channel impulse response reconstruction is the emerging reconfigurable intelligent surfaces [15].There has been much work in the past few years toward mmWave massive MIMO channel characterization and reconstruction either by measurement [16] or ray-tracing computation [13] towards providing channel impulse response models for various application scenarios.

The millimeter-wave spectrum, which is between 30 GHz and 300 GHz, is the second main technology for achieving a higher data throughput and ultra-reliable low latency communication [10,-11]. Numerous mmWave bands seem promising. These include the E-band at 71-76 GHz, 81-86 GHz, and 92-95 GHz, as well as the local multi-point distribution service at 28-30 GHz [19]. Multi-Gbps transmission rates are made possible by the vast quantity of spectrum that is available at mmWave frequencies [20]. However, mmWave frequencies have some drawbacks, such as the ease with which obstructions can block mmWave signals, limiting direct Line-of-Sight (LOS) communications. Additionally, the propagation performance is diminished by the deep shadow zones brought on by the higher diffraction loss at mmWave [21]. The mmWave channel seems to mobile users to be quite variable as a result of the foregoing. Therefore, a modeling approach that works for the mmWave channel is required. A realistic collection of channel models, for numerous use case situations, must first be constructed in order to adequately evaluate competing air interfaces and beam alignment techniques for mmWave communications. These channel models must include characteristics like pathloss, distant-dependent rms delay spread, and distant-dependent azimuth/elevation angle spreads of departure and arrival that are identical to the 3D channel model defined in 3GPP [22].

1.1. 3D Channel Model

In channel modeling and reconstruction, the channel matrix otherwise called the channel impulse response contains all the channel multipath components of interest that is needed to model the channel, it is therefore important to derive channel equation with the aim of identifying the contributing parameters necessary for the 2D and 3D model. Assuming N clusters of multipath rays from scatterers exist between the base station and the receiver where each cluster is made up of one resolvable propagation path and delay τ. In consideration of figure 2, if the perpendicular axis to the X-Y plane is taken as the elevation domain. Let the complex envelop of the transmitted single input single output (SISO) signal (baseband signal) be represented as $\tilde{S}(t)$ while the real part of the transmitted bandpass signal $S(t)$ is:

$$S(t) = Re\left[\tilde{S}(t)e^{j2\pi f_c t}\right] \tag{1}$$

where the signal phase is given as $j2\pi f_c t$. The received noiseless bandpass signal after Doppler effect and delay due to transmission is given as:

$$r(t) = Re\left[\sum_{l=1}^{L} \alpha_l e^{j2\pi(f_c+f_{D,l})(t-\tau_l)}\tilde{S}(t-\tau_l)\right] \tag{2}$$

Expanding $(f_c + f_{D,l})(t-\tau_l)$ in Equation (2) and rearranging, we have

$$r(t) = Re\left[\sum_{l=1}^{L} \alpha_l e^{j2\pi[f_{D,l}t-(f_c+f_{D,l})\tau_l]}\tilde{S}(t-\tau_l)e^{j2\pi f_c t}\right] \tag{3}$$

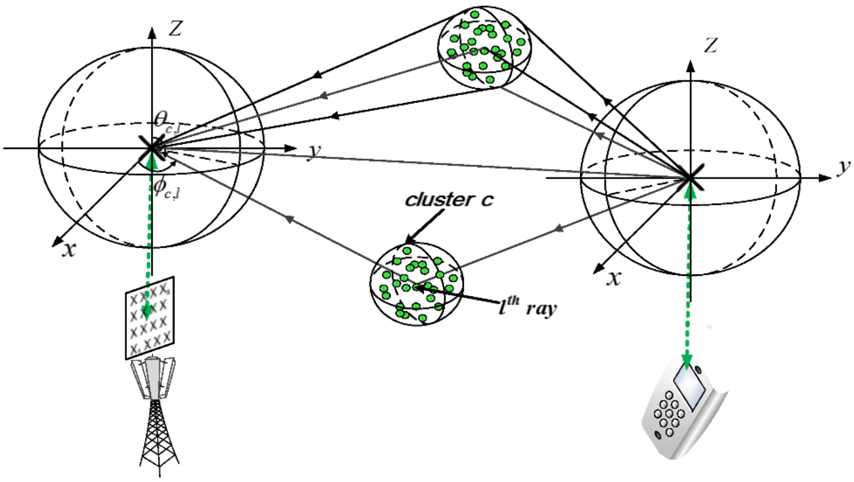

Fig. 2. MIMO 3D Generic Channel Model [23]

Where α_l is the channel attenuation factor, f_c is the carrier frequency, $f_{D,l}$ is the doppler shift for the l^{th} multipath component (MPC), and τ_l is the delay of the l^{th} MPC. Comparing equations (1) and (3), we see that $\tilde{S}(t)$ in (1) is in (3) equivalent to:

$$\tilde{S}(t) = \sum_{l=1}^{L} \alpha_l e^{j2\pi[f_{D,l}t-(f_c+f_{D,l})\tau_l]}\tilde{S}(t-\tau_l) \tag{4}$$

From Equation (4), let the phase of the MPC associated with the l^{th} path be given as:

$$\emptyset_l = 2\pi\left[f_{D,l}t - (f_c + f_{D,l})\tau_l\right]$$

where $\emptyset_l$ is distributed between $[0, 2\pi]$ showing that a slight change in τ due to movement within the channel results in a significant phase shift. Equation (3), the received passband signal thus becomes:

$$r(t) = Re\left[\sum_{l=1}^{L} \alpha_l e^{j\emptyset_l(t)}\tilde{S}(t-\tau_l)e^{j2\pi f_c t}\right] \tag{5}$$

where the received baseband signal is given as:

$$\tilde{r}(t) = \sum_{l=1}^{L} \alpha_l e^{j\emptyset_l(t)}\tilde{S}(t-\tau_l) \tag{6}$$

Substituting Equation (6) into Equation (5), thus:

$$r(t) = Re[\tilde{r}(t)e^{j2\pi f_c t}] \tag{7}$$

Every transmitted signal through the propagation channel experiences attenuation and delay termed its channel impulse response. The impulse response for the l^{th} MPC can be extracted from (6) as in [24]:

$$h(t, \tau_l) = \alpha_l e^{j\phi_l(t)} \tag{8}$$

Substituting Equation (8) into Equation (6), we have Equation (6) as:

$$\tilde{r}(t) = \sum_{l=1}^{L} h(t, \tau_l)\tilde{S}(t - \tau_l) \tag{9}$$

Using convolution principle, Equation (9) becomes:

$$\tilde{r}(t) = h(t, \tau) * \tilde{S}(t) \tag{10}$$

where the channel impulse response is given as:

$$h(t, \tau) = \sum_{l=1}^{L} h(t, \tau_l).\delta(t - \tau_l) \tag{11}$$

Equation (11) is a 2D channel model and can be extended to a 3D model by including the elevation angles at the arrival and departure. A general CIR time-domain model can then be written as in [25]:

$$h(\tau, \theta) = \sum_{l=1}^{L} h(t, \tau_l).\delta(t - \tau_l).\delta(\theta - \theta_l) \tag{12}$$

where $\delta(t - \tau_l)$ is the time of arrival impulse, and $\delta(\theta - \theta_l)$ is the angle of arrival impulse

From (11), the MIMO CIR matrix of all paths at time t is given as in [26]:

$$H(t, \tau) = \sum_{l=1}^{L} H_l(t).\delta\,(t - \tau_l) \tag{13}$$

$H_l(t)$ is the $N_{SBS}\ X\ N_{MBS}$ mmWave-MIMO propagation channel matrix of the l^{th} multipath ray between the transmit antenna N_{MBS} and the receive antenna N_{SBS}, H_l is a narrow band modified block-fading channel model which embraces the sparse scattering nature of mmWave channels. In the standardized ITU-R M.2135 2D channel model [27], the channel response of each propagating path in the propagating channel matrix $H_l(t)$ depends on a set of parameters. The parameters include the Doppler shift υ, the delay τ, the departure/arrival $angles\ \phi_{l,n}$ and $\varphi_{l,n}$, and the polarization matrix $\Lambda_{l,n}^{2D}$. If we consider a single path, the CIR for the resulting 2D model from transmit antenna n_{mbs} to receive antenna n_{sbs} for path *l* is given as [26];

$$H_{n_{sbs},n_{mbs},n}^{2D}(t) = \sqrt{P}_n \sum_{l=1}^{L} \left[\Gamma_{rx,n_{sbs}}^{2D}\left(\varphi_{rx,l,n}\right)\right]^T \Lambda_{l,n}^{2D} \left[\Gamma_{tx,n_{mbs}}^{2D}\left(\phi_{tx,l,n}\right)\right].exp\left\{j2\pi v_{l,n} t\right\} \tag{14}$$

To extend the 2D model to the 3D model, the ULA antenna array is replaced with a 2D grid UPA antenna array to obtain the elevation angle required to obtain the correlation of the antenna array in the elevation domain. Thus, the 3D-MIMO channel model is defined in cylindrical coordinates, the 3D CIR of the n^{th} cluster from the transmit antenna n_{mbs} to the receive antenna n_{sbs} is expressed as [26]

$$\begin{aligned} H_{n_{sbs},n_{mbs},n}^{3D}(t) = \sqrt{P}_n \sum_{l=1}^{L} \left[\Gamma_{rx,n_{sbs}}^{3D}\left(\psi_{rx,l,n}\right)\right]^T \Lambda_{l,n}^{3D} \left[\Gamma_{tx,n_{mbs}}^{3D}\left(\psi_{tx,l,n}\right)\right].exp\left\{j2\pi\lambda^{-1}\left(\bar{\varphi}_{l,n}.\bar{d}_{rx,n_{sbs}}\right)\right\} \\ .exp\left\{j2\pi\lambda^{-1}\left(\bar{\phi}_{l,n}.\bar{d}_{tx,n_{mbs}}\right)\right\}.exp\left\{j2\pi v_{l,n} t\right\}) \end{aligned} \tag{15}$$

where superscript 3D shows that the transmitted wave propagates in 3D space, and the subscripts l and n stand for the number of multipath and cluster, respectively, $\Gamma_{rx,n_{sbs}}^{3D}$ indicate the full 3D pattern of the receive antenna n_{sbs}, in the V and H polarization. $\Gamma_{tx,n_{mbs}}^{3D}$ specify the full 3D pattern of the transmit antenna n_{mbs} in the V and H polarization. $\psi_{rx,l,n}$ and $\psi_{tx,l,n}$ are the n^{th} cluster and l^{th} multipath/ray angle of arrival and departure, respectively, in the 3D domain. $\Lambda_{l,n}^{3D}$ is the 3D polarization matrix specified by vertical polarization component V and horizontal polarization component H. The location vector of the receive antenna element n_{sbs} and transmit antenna element n_{mbs} are denoted by $\bar{d}_{rx,n_{sbs}}$, and $\bar{d}_{tx,n_{mbs}}$, respectively. $\sqrt{P}_n$ is the power of the n^{th} cluster. Finally, $v_{l,n}$ specifies the Doppler shift (which is zero: fixed small cells) in this work. For 3D fading channel models, both azimuth and elevation angles characterize the multipath components, therefore breaking the arrival and departure angles in Equation (15) into the azimuth and elevation domain, the azimuth angle of departure and arrival is thus represented by $\phi_{l,n}$, and $\varphi_{l,n}$. In contrast, the elevation angle of departure and arrival are represented by $\theta_{l,n}$, and $\vartheta_{l,n}$, respectively. $F_{rx,n_{sbs},V}$ and $F_{rx,n_{sbs},H}$ is the small cell (sbs^{th}) field antenna patterns in 3D for the theta (vertical, V) and phi (horizontal, H) polarizations, respectively. $\Phi_{l,n}^{vv}$ is the phase value for the vv (vertical-vertical) polarization, while the other three are for $vh, hv,$ and hh polarization combinations. The spherical unit vector in the direction of azimuth and elevation angles of departure and arrival are represented by $\bar{\varphi}_{l,n}$, and $\bar{\phi}_{l,n}$, respectively. $\bar{d}_{rx,n_{sbs}}$, and $\bar{d}_{tx,n_{mbs}}$ are the location vector of receive small cell antenna element n_{sbs} and transmit antenna element. n_{mbs}, respectively with ƙ being the cross-polarization power ratio in a linear scale and P_n is the power of cluster (n). Therefore, from Equation (15), the angles of elevation and azimuth et ectara earlier defined, we have that

$\psi_{rx,l,n} = \varphi_{l,n}, \vartheta_{l,n}$, $\psi_{tx,l,n} = \phi_{l,n}, \theta_{l,n}$, $\Lambda_{l,n}^{3D} = \begin{bmatrix} e^{j\Phi_{l,n}^{vv}} & \sqrt{ƙ_{l,n}^{-1}} e^{j\Phi_{l,n}^{vh}} \\ \sqrt{ƙ_{l,n}^{-1}} e^{j\Phi_{l,n}^{hv}} & e^{j\Phi_{l,n}^{hh}} \end{bmatrix}$ while $\Gamma_{rx,n_{sbs}}^{3D} = \begin{bmatrix} F_{rx,n_{sbs},V} \\ F_{rx,n_{sbs},H} \end{bmatrix}$ and $\Gamma_{tx,n_{mbs}}^{3D} = \begin{bmatrix} F_{tx,n_{mbs},V} \\ F_{tx,n_{mbs},H} \end{bmatrix}$. Slotting all the parameters into Equation (15) without the Doppler component can thus be expanded as in [28]:

$$H_{n_{sbs},n_{mbs},n}^{3D}(t) = \sqrt{P_n} \sum_{l=1}^{L} \begin{bmatrix} F_{rx,n_{sbs},V}(\varphi_{l,n}, \vartheta_{l,n}) \\ F_{rx,n_{sbs},H}(\varphi_{l,n}, \vartheta_{l,n}) \end{bmatrix}^T . \begin{bmatrix} e^{j\Phi_{l,n}^{vv}} & \sqrt{ƙ_{l,n}^{-1}} e^{j\Phi_{l,n}^{vh}} \\ \sqrt{ƙ_{l,n}^{-1}} e^{j\Phi_{l,n}^{hv}} & e^{j\Phi_{l,n}^{hh}} \end{bmatrix} \begin{bmatrix} F_{tx,n_{mbs},V}(\phi_{l,n}, \theta_{l,n}) \\ F_{tx,n_{mbs},H}(\phi_{l,n}, \theta_{l,n}) \end{bmatrix}$$
$$. exp\{j2\pi\lambda^{-1}(\bar{\varphi}_{l,n}. \bar{d}_{rx,n_{sbs}})\}. exp\{j2\pi\lambda^{-1}(\bar{\phi}_{l,n}. \bar{d}_{tx,n_{mbs}})\} \quad (16)$$

1.2. Literatre Review

For mmWave communications, a number of channel models have been proposed, such as [29], which was conducted at 32 GHz for an indoor office environment. The authors of [30] created a model for a street canyon environment in the 70–80 GHz band. However, the work was only done in the azimuth domain; as a result, it was improved in [31], where a 3D ray tracing technique was used to extend the model to 3D and include elevation spread for use in system level simulation. By incorporating polarization, angle biases, and non-line-of-sight connectivity, the work of [22] enhanced the work of [31]. The authors of [32] used the New York University (NYU) Wireless measurement equipment to develop a mmWave large-scale path loss model for line of sight and non-line of sight at 28 GHz and 73 GHz frequency band, while the authors of [33] presented a set of mmWave radio propagation parameters based on both measurement and ray-tracing techniques. The 3GPP spatial channel model was used to create the channel models (SCM). The authors of [34] proposed a 3D mmWave indoor directed and omnidirectional channel model based on in-depth radio propagation data at 28 and 140 GHz. The authors of [35] used 3D ray-tracing at 28 GHz to examine path loss, free space path loss with and without antenna pattern, and excess path loss with and without antenna pattern for a city environment. The authors then used a root mean square error, a close-in (CI) model, and a floating intercept (FI) path loss model to build the ideal path loss model for Lagos Island (RMSE). In the work of [36], the authors provided a mathematical model for unmanned aerial vehicles (UAV) which added the UAV in both military and civilian deployment.

There are different techniques of channel reconstruction including the use of geometry-aided angles of arrival estimation [14] where the channel is reconstructed using the estimate of the azimuth and elevation angles of arrival. The authors of [9] used uplink reciprocity CSI combined with limited feedback in a frequency division duplexing (FDD) system, where the gains, delay, and angles are estimated during uplink sounding. The BS can then use the information to reconstruct the downlink channel. In the work of [16] a neural network-based deep learning compressed sensing channel estimation scheme is used to predict the beamspace channel amplitude. The channel is then reconstructed based on the obtained indices of dominant beamspace channel entries. The authors of [37] reconstructed full downlink MIMO CSI at the BS using uplink-sounding reference signals and quantized downlink CSI from practical antenna structures with reduced downlink CSI-RS overhead. The authors of [38] propose a Path Clustering based Channel Reconstruction (PCCR) scheme for channel reconstruction to solve the problem of CSI measurement. By leveraging channel information parameters such as angle of arrival, angle of departure, etc. at a number of geographical locations that are recorded in the Channel Path Map (CPM) which are used to reconstruct the channel while the authors of [39] propose to employ the trigonometric interpolation technique to reconstruct the mmWave spatial channel profile (power-angle-delay profile, composite power angular spectrum delay and angle characteristics).

Since mmWave wireless communication for 5G and beyond is still a growing research area, there is a lack of information, including accurate elevation statistics, particularly for angle of departure at the base station. In this article, we propose a mmWave channel model that aims to improve the channel model of [33]. Our work focuses on the characterization of mmWave propagation models, including both 3D angular-domain channel parameters and delay-domain channel parameters, to enable bi-directional broadband channel reconstruction for LOS and NLOS in the Street

Canyon and High-rise scenarios. The contribution of the proposed channel estimation method based on channel reconstruction using the parameters of the models developed includes its potential to provide more detailed information about the channel characteristics, such as delay, angular spread, and interference, ensuring data transmission without errors and interference. Therefore, this method can help to estimate the channel of mmWave massive MIMO systems.

The rest of this work is arranged as follows. Section one is the introduction, section two is the methodology while section three deals with the result and discussions. We conclude in section four.

2. Methodology

The research method used in this work is to achieve the purpose of channel parameter extraction needed to model and reconstruct the channels. The Wireless Insite ray tracing simulation algorithm was used. The simulations were conducted in a virtual environment, using the digital map of Lagos Island, Nigeria, with dimensions 500m x 500m. The transmitter is located a bit offset from the middle of the coverage area. The outdoor-to-indoor (O2I) high-rise and urban microcell (UMi) street canyon scenarios are taken into consideration. The signal is sent in this instance from the outdoor base station erected on a 10 m tower to small cells placed on each level of a 30-floor building, with 3.5 m spacing on floor-by-floor (vertical spacing), giving a total of 105 m building height. This 30-storey structure is located in a densely populated area. The small cell receivers are arranged along Broad Street with a 2.5 m height and a 1 m spacing in the UMi street canyon scenario. A length of 600 m is covered by the 600 small cells that have been deployed overall. The BS employs beamforming with adaptive modulation and maximum ratio transmission (MRT) with 32 MIMO transmitter antennas. A 4 MIMO receiver antenna and maximum ratio combining (MRC) are both features of each small cell, in contrast, which is how they detect signals. The digital 3D environment map can be found in Figure 3. The various simulation settings and their values are displayed in Table 1. For the simulation procedure, a 3D geometric digital map made up of three files—a city file, an image file, and a terrain file—was loaded onto the Wireless Insite ray tracing engine to create the propagation environment. Next, a 4 x 4 dual-polarized MIMO transmitter antenna and a 2 x 2 MIMO receiver antenna were built using a narrowband sinusoidal 28 GHz waveform with a bandwidth of 100 MHz for the simulation to determine MIMO channel characteristics. To study the behavior of the channel parameters using the characteristics of their probability distribution functions (PDFs), the dataset for each parameter was imported into MATLAB, 2017b. To create the best fit PDF of the dataset, the distribution fitter application found in the statistics and machine learning toolbox was employed. Then, the statistics (mean and variance) of each parameter's PDF that described how that parameter behaved were collected.

Table 1. Parameters for the simulation

Simulation Parameters	Values
Number of small cells in street canyon	600
Number of small cells in high rise	30
Carrier Frequency	28 GHz
Bandwidth	100 MHz
Transmit power of BS	30 dBm
Height of BS	10m
Small cell height in street	2.5m
Small cell height in high rise	various
Antenna BS	4 x 4 UPA
Small cell antenna	2 x 2
Antenna element spacing	1 wavelength
Number of Max reflections	6
Max diffraction	1
Max penetration number	1

Having obtained the large-scale channel parameters of angular spread and delay spread using the Wireless Insite Ray tracing simulation, other LSPs such as the shadow fading (SF) were generated using algorithm 1. Algorithm 2 was used to generate the small-scale channel parameters such as the cluster power, azimuth/elevation angles of arrival and departure for both the LOS and NLOS as well as the polarization power ratio. The LSPs and SSPs were used as input in algorithm 3 to generate the channel coefficients which are needed for the channel reconstruction.

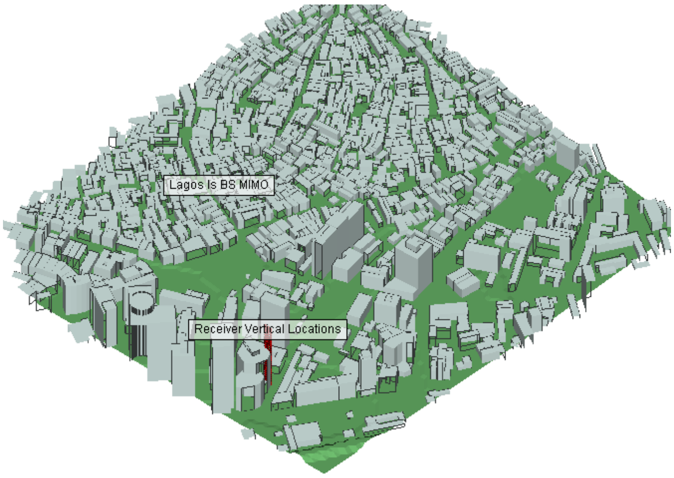

Fig. 3. Digital 3D Map of the Virtual Environment of Data Collection

2.1. Data Collection and Analysis Techniques

For data collection and analysis, the following datasets were collected as CSV files for each of the 600 small cells in the street canyon scenario and 30 small cells in the high-rise scenario; azimuth angle of arrival, azimuth angle of departure, elevation angle of arrival, elevation angle of departure, azimuth spread of arrival, azimuth spread of departure, elevation spread of arrival, elevation spread of departure, delay spread etc. These were then preprocessed and cleansed. Using the statistics and machine learning toolbox in MATLAB, we generated various best-fit models of those datasets. We extracted the statistics of their probability density functions (pdf) which were used in the various algorithms to reconstruct the channel state information for the LOS and NLOS of the two scenarios.

2.2. Reconstruction Method for 3D Channel Model

Based on the ray-tracing data and obtained parameter values, a mmWave channel model for the O2I and the UMi scenarios reconstructed using the procedures outlined in 3GPP TR 36.873 release 12 [40] is proposed. Figure 4 shows the steps to realizing the 3-D channel model. After the channel parameter acquisition through ray tracing, post processing and data analysis was performed and the mmWave massive MIMO matrix generation and channel simulation were performed. Figure 4 shows the steps in achieving the 3D channel parameter acquisition leading to the 3D channel model.

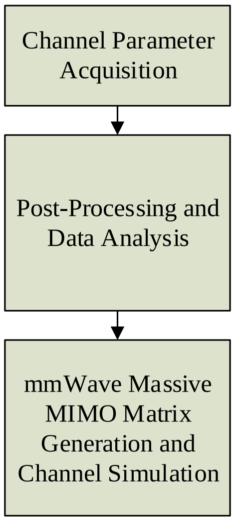

Fig. 4. Steps to Realizing 3-D Channel Model

1. Set up simulation environment using the 3D digital map of Lagos Island in Wireless Insite ray-tracing engine (determine SBS and MBS location, antenna array configuration, select 3D-UMi NLOS for street canyon and 3D-UMi O2I for high-rise, etc.)
2. Select NLOS propagation condition.
3. Calculate Omni-directional path-loss using [41]

$$PL[dB](d) = PL(d_0)dB + 10n_{pl}log_{10}(d) + \sigma_{SF}$$

Where $PL(d_0)dB$ is 296dB,n_{pl} is the path loss exponent (2.309), d is the distance in meters, and σ_{SF} is the shadow fading std (56.24) for NLOS.

4. Produce the large-scale parameters of rms delay spread, rms azimuth spread of arrival, rms elevation spread of arrival, etc., using table 3 to generate and cross-correlate them. Here, we generate five large-scale parameters and then correlated them. We limit AOA/AOD spread (ASA/ASD) to 100^0 and EOA/EOD (ESA/ESD) to 40^0.
5. Generate delays that are drawn from the delay distribution defined in table 3 with Lognormal distribution. Calculate τ_n' where r_τ is the delay scaling factor given as 3. [22], σ_τ is the standard deviation of the distribution, and X_n is a unit-variance Gaussian RV

$$\tau_n' = -r_\tau \sigma_\tau ln X_n$$

We normalize the delays by subtracting the minimum delay from every other delay value and sort the result in descending order such that:

$$\tau_n = sort\left(\tau_n' - min(\tau_n')\right)$$

6. Produce the cluster power as:

$$P_n' = exp\left(-\tau_n \frac{r_\tau - 1}{r_\tau \sigma_\tau}\right) . 10^{-0.1Z_n}$$

where $Z_n N(0, \beta^2)$, and β is the per cluster shadow fading term in dB given as 5 [22]. Normalize power such that the sum of all cluster power is one. i.e.

$$P_n = \frac{P_n'}{\sum_{n=1}^{N} P_n'}$$

7. Produce the azimuth angles of arrival and departure as shown below. The AOAs and AODs are governed by applying the inverse Gaussian function below with cluster power P_n and rms elevation spread of arrival and departure σ_{ASA} and σ_{ASD}, respectively, as input (after applying a scaling factor of 1.018 for 8 clusters) [40].

$$\varphi_{n,AOA} = 1.96(\sigma_{ASA}/1.4)\sqrt{-ln(P_n/max(P_n))}$$
$$\phi_{n,AOD} = 1.96(\sigma_{ASD}/1.4)\sqrt{-ln(P_n/max(P_n))}$$

8. Produce the elevation angles of arrival and departure as shown below. The EOAs and EODs are governed by applying the inverse Gaussian function below with cluster power P_n and rms elevation spread of arrival and departure σ_{ESA} and σ_{ESD}, respectively, as input (after applying a scaling factor of 1.104 for 12 clusters) [40].

$$\vartheta_{n,EOA} = -0.906\sigma_{EOA} ln\left(\frac{P_n}{max(P_n)}\right)$$
$$\theta_{n,EOD} = -0.906\sigma_{EOA} ln\left(\frac{P_n}{max(P_n)}\right)$$

9. By randomly ordering each set of angles inside a cluster (for example, using MATLAB's randperm (10) within each group of angles within a cluster), we couple all rays within a cluster, i.e., couple AOD, AOA, EOA, and EOD angles. Produce the cross-polarization power, XPRs as $\kappa_{l,n} = 10^{X/10}$ where X is Gaussian distributed.
10. Produce the random phase values for all four polarization combination terms, $\Phi_{l,n}^{vv}$, $\Phi_{l,n}^{vh}$, $\Phi_{l,n}^{hv}$, $\Phi_{l,n}^{hh}$.

After the LSPs modeling, we propose an iterative algorithm (Algorithm 1) to generate the LSP needed for 3D channel reconstruction.

Algorithm 1: Algorithm for Large Scale Parameter (LSP) Generation

Input: Network layout and antenna/user equipment configuration
Output: Large scale parameters
Initialization:

Assuming K links with K users located at (x_k, y_k) and each channel link has M large scale parameters. $N = M * K$ lognormal large scale parameter variables that correlate with each other are generated.

While simulation scenario active **do**

Generate correlation matrix $(C) = N \times N$

Generate N LSPs by multiplying the square root of the correlation matrix $(\sqrt{C})$ by the column matrix $(N \times 1)$

Calculate the inter-station correlation for each LSP using the correlation distance

Find the modified shadow fading(SF) as: $SF = \sqrt{\frac{2\sigma_{SF}^2}{M}} \sum_{m=1}^{M} \sin(\overline{D}.\overline{\beta_m} + \theta_m)$

Get the M LSPs for the $k - th$ User Equipment using linear transformation as:

$$\tilde{S}(x_k, y_k) = \sqrt{C_{m\times m}(0)}\zeta(x_k, y_k)$$

End

Where
M – number of sinusoids
σ_{SF}^2 – the target standard deviation
$\overline{D}$ – the 6D coordination vector of the transmitter and receiver
$\underline{\theta_m}$ – uniformly distributed random phase in $(0, 2\pi)$
$\overline{\beta_m}$ – the $m - th$ wave vector

We also propose an iterative algorithm (Algorithm 2) to generate the small scale parameters SSP needed for 3D channel reconstruction

Algorithm 2: Algorithm for Small Scale Parameter (SSP) Generation

Input: Network layout and antenna/user equipment configuration
Output: Small scale parameters
Initialization:
Keep track of multi-path components.
While simulation scenario active **do**

1. Estimate the relative delay of multi-path τ: $\tau_n' = -r_\tau \sigma_\tau \ln(X_n)$. A total of N cluster delays are generated.
2. Sort delays in ascending order; $\tau_n = sort(\tau_n' - \min(z_n'))$
3. For LOS, adjust the delay sorting to $\tau_n^{LOS} = \frac{\tau_n}{c_{DS}}$
4. Generate cluster power P assuming a single slope exponential power delay profile:
$$P_n' = exp\left(-T_n \frac{r_\tau - 1}{r_\tau \sigma_\tau}\right). 10^{-\frac{CSF_n}{10}}$$
5. For LOS, adjust the cluster power P to: $P_n = \frac{P_n'}{\sum_{n=1}^{N} P_n'}$; $P_n^{LOS} = \frac{1}{KF+1} P_n + \delta(n - 1)P_{1,LOS} = \frac{1}{KF+1} P_n + \delta(n-1)\frac{KF}{KF+1}$.
6. If even cluster has M_n rays, then the power of each ray within each cluster n is expressed as $\frac{P_n}{M_n}$.
7. Generate angle of arrival (AOA) using the inverse Gaussian function:
$$AOA = \hat{\varphi}_{n,AOA} = \frac{ASA}{0.7C_{AS}} \sqrt{-\ln\left(\frac{P_n}{max(P_n)}\right)}$$
8. For LOS and NLOS clusters:
$$\varphi_{n,AOA} = \begin{cases} X_n \hat{\varphi}_{n,AOA} + y_n + \varphi_{LOS,AOA} , & NLOS \\ X_n \hat{\varphi}_{n,AOA} + y_n - X_1 \hat{\varphi}_{1,AOA} - y_1 + \varphi_{LOS,AOA}, & LOS \end{cases}$$
9. The AOA for ray n, m:
$$\varphi_{n,m,AOA} = \varphi_{n,AOA} + CASA.\alpha_m$$
10. Generate angle of departure (AOD) using the inverse Gaussian function:
$$AOD = \hat{\theta}_{n,AOD} = \frac{ASD}{0.7C_{AS}} \sqrt{-\ln\left(\frac{P_n}{max(P_n)}\right)}$$

11. For LOS and NLOS clusters:

$$\theta_{n,AOD} = \begin{cases} X_n\hat{\theta}_{n,AOD} + y_n + \theta_{LOS,AOD}\ , & NLOS \\ X_n\hat{\theta}_{n,AOD} + y_n - X_1\hat{\theta}_{1,AOD} - y_1 + \theta_{LOS,AOD}, & LOS \end{cases}$$

12. The AOD for ray n, m:

$$\theta_{n,m,AOD} = \theta_{n,AOD} + CASA.\alpha_m$$

13. Generate Zenith angle of arrival (ZOA) and

$$ZOA = \hat{\varphi}_{n,ZOA} = -\frac{ZSA}{C_{ES}}\ln\left(\frac{P_n}{max(P_n)}\right)$$

14. For LOS and NLOS clusters:

$$\varphi_{n,ZOA} = \begin{cases} X_n\hat{\varphi}_{n,ZOA} + y_n + \varphi_{ZOA}, & NLOS \\ X_n\hat{\varphi}_{n,ZOA} + y_n - X_1\hat{\varphi}_{n,ZOA} - y_1 + \varphi_{ZOA}, & LOS \end{cases}$$

15. The ZOA for ray n, m:

$$\varphi_{n,m,ZOA} = \varphi_{n,ZOA} + CZSA.\alpha_m$$

16. Generate Zenith angle of departure (ZOD) and
17. For LOS and NLOS clusters:

$$\theta_{n,ZOD} = \begin{cases} X_n\hat{\varphi}_{n,ZOD} + y_n + \mu_{offset,ZOD} + \theta_{LOS,ZOD}, & NLOS \\ X_n\hat{\theta}_{n,ZOA} + y_n - X_1\hat{\theta}_{n,ZOD} - y_1 + \theta_{LOS,ZOD}, & LOS \end{cases}$$

18. The ZOD for ray n, m:

$$\theta_{n,m,ZOD} = \theta_{n,ZOD} + \frac{3}{8}10^{\mu}ZSD.\alpha_m$$

19. Generate cross polarization power ratio (XPR) of each ray within a cluster as a lognormal distribution:

$$K_{n.m} = 10^{X/10}$$

End

Where
τ_n' - is the absolute delay of the nth cluster
r_τ – the standard deviation of delay distribution σ_{delays} over delay spread σ_τ : $r_\tau = \frac{\sigma_{delays}}{\sigma_\tau}$
$C_{DS}, C_{AS,} C_{DS}$ – scaling factors relating to the number of clusters
CSF_n – per-cluster shadow fading
$K - F$- Ricean K-factor
$\delta(n)$ – dirac delta function or impulse response
ASA – RMS azimuth angle of spread of arrival
$CASA$ – RMS azimuth angle of spread of arrival of each cluster
$CZSA$ – RMS zenith angle of spread of arrival of each cluster
α_m – offset angles of mth ray
P_n - average power
y_n – Gaussian random variable with zero mean and a variance of $\left(\frac{ASA}{7}\right)^2$
X_n – channel parameters (set to $-1\ or + 1$)
$X \sim N(\mu, \sigma^2)$
μ – mean
σ^2 - variance

All parameters are compiled together in Table 2 for simulation of channel coefficient for channel reconstruction.

Table 2. Parameter for Simulation of Channel Reconstruction

Parameter(s)	Model Statistics	Urban Microcell Environment			
		Street Canyon Scenario		Urban High-Rise Scenario	
		LOS	NLOS	LOS	NLOS
Delay Spread (s)	μ	N/A	40.89	N/A	69.04
	σ	N/A	5.76	N/A	20.63
AOD Spread (degrees)	μ	N/A	3.36	N/A	3.77
	σ	N/A	0.52	N/A	0.25
AOA Spread (degrees)	μ	N/A	1.99	N/A	3.5
	σ	N/A	0.96	N/A	0.12
Shadow Fading (dB)	μ	36.26	56.24	36.26	56.25
	σ				
K-factor (dB)	μ	9	N/A	N/A	N/A
	σ	2	N/A	N/A	N/A

Cross-Correlation	RMS ESD vs. RMS ASD	N/A	0.05	N/A	0.34
	RMS ESA vs. RMS ASD	N/A	-0.1	N/A	0.34
	RMS ESD vs. RMS ASA	N/A	0.17	N/A	-0.25
	RMS ESA vs. RMS ASA	N/A	0.14	N/A	-0.47
	RMS ASD vs. RMS ASA	N/A	0.37	N/A	-0.8
	RMS ESD vs. RMS ESA	N/A	0.96	N/A	0.72
	RMS DS vs. RMS ASA	N/A	0.46	N/A	-0.1
	RMS DS vs. RMS ASD	N/A	0.58	N/A	0.35
	RMS DS vs. RMS ESA	N/A	-0.15	N/A	0.47
Delay Scaling Parameter		3	N/A	3	N/A
XPR (dB)		15	15	15	15
Number of Clusters		1	2	1	3
Number of rays per cluster		8	12	8	12
Cluster ASD		6	6	6	6
Cluster ASA		5.2	5.2	5.2	5.2
Per Cluster Shadowing Std in (dB)		5	5	5	5
Correlation Distance (m)	DS				
	ASD				
	ASA				
	SF				
	K	9	N/A	N/A	N/A

Results of various parameter values as shown in Table 3 which were derived from algorithms 1 and 2 were used in algorithm three for simulation of channel coefficient for channel reconstruction.

Algorithm 3: Generation of Channel Coefficients

Input: Large scale parameters, small scale parameters

Output: Channel coefficients

Initialization:

Keep track of measured parameters.

While simulation scenario active **do**

1. Get the four polarization pairs of ray $n.m$ $(\theta\theta, \theta\varphi, \varphi\theta, \varphi\varphi)$
2. Generate channel coefficients for each cluster n and each receive and transmit element u and s respectively.
3. Plot the channel coefficients of all clusters excluding the two strongest clusters $(N-2)$

$$H_{u,s,n}^{NLOS}(t;\tau) = \sqrt{\frac{P_n}{M}} \sum_{m=1}^{M_n} \begin{bmatrix} F_{rx,u,\theta}(\theta_{n,m,ZOA}, \ \varphi_{n,m,AOA}) \\ F_{rx,u,\varphi}(\theta_{n,m,ZOA}, \ \varphi_{n,m,AOA}) \end{bmatrix}^T \begin{bmatrix} e^{j\emptyset_{n,m}^{\theta\theta}} & \sqrt{K_{n,m}^{-1}} e^{j\emptyset_{n,m}^{\theta\varphi}} \\ \sqrt{K_{n,m}^{-1}} e^{j\emptyset_{n,m}^{\varphi\theta}} & e^{j\emptyset_{n,m}^{\varphi\varphi}} \end{bmatrix}$$
$$\times \begin{bmatrix} F_{tx,s,\theta}(\theta_{n,m,ZOD}, \ \varphi_{n,m,AOD}) \\ F_{tx,s,\varphi}(\theta_{n,m,ZOD}, \ \varphi_{n,m,AOD}) \end{bmatrix}$$
$$\times e^{\left(j2\pi\lambda_o^{-1}\left(T_{rx,n,m}(\bar{d}_{rx,u}+\bar{V}_{rx}^{t})+T_{rx,n,m}(\bar{d}_{tx,s}+\bar{V}_{tx}^{t})\right)\right)} \delta(\tau - \tau_{n,m})$$

4. Plot the channel coefficients of the two strongest clusters.

$$H_{u,s,n}^{LOS}(t) = \sqrt{\frac{1}{KF+1}} H_{u,s,n}^{NLOS}(t) + \delta(n-1)\sqrt{\frac{KF}{KF+1}} \begin{bmatrix} F_{rx,u,\theta}(\theta_{n,m,ZOA}, \ \varphi_{n,m,AOA}) \\ F_{rx,u,\varphi}(\theta_{n,m,ZOA}, \ \varphi_{n,m,AOA}) \end{bmatrix}^T \times \begin{bmatrix} e^{j\emptyset_{LOS}} & 0 \\ 0 & e^{j\emptyset_{LOS}} \end{bmatrix}$$
$$\times \begin{bmatrix} F_{tx,s,\theta}(\theta_{n,m,ZOD}, \ \varphi_{n,m,AOD}) \\ F_{tx,s,\varphi}(\theta_{n,m,ZOD}, \ \varphi_{n,m,AOD}) \end{bmatrix}$$
$$\times e^{\left(j2\pi\lambda_o^{-1}\left(T_{rx,LOS}(\bar{d}_{rx,u}+\bar{V}_{rx}^{t})+T_{rx,LOS}(\bar{d}_{tx,s}+\bar{V}_{tx}^{t})\right)\right)}$$

End

Where:
s - transmitting antenna element
u – receiving antenna element
$H_{u,s,n}(t;\tau)$ – dynamic sub-channel from transmitting antenna to receiving antenna with channel parameters that are time-varying.
N - number of clusters between transmitting antenna element and receiving antenna element
M_n – the number of rays in the $n-th$ cluster
$F_{tx,s,\theta}$; $F_{tx,s,\varphi}$ – the elevation angle and azimuth radiation field pattern of transmitting antenna element, s.
$F_{rx,u,\theta}$; $F_{rx,u,\varphi}$ – the elevation angle and azimuth radiation field pattern of receiving antenna element, u.
$\emptyset_{n,m}^{\theta\theta}, \emptyset_{n,m}^{\theta\varphi}, \emptyset_{n,m}^{\varphi\theta}, \emptyset_{n,m}^{\varphi\varphi}$ – the complex gains of the four polarization pairs of the $m-th$ ray in cluster n.
$\theta\theta$ – elevation-elevation polarization pairs
$\theta\varphi$ – elevation-azimuth polarization pairs
$\varphi\theta$ – azimuth-elevation polarization pairs
$\varphi\varphi$ – azimuth-azimuth polarization pairs
the angle of arrival (AOA) of ray (n,m) containing elevation angle of arrival (EOA) $(\theta_{rx,n,m})$ and azimuth angle of arrival (AoA) $(\varphi_{rx,n,m})$.
the angle of departure (AOD) of ray (n,m) containing elevation angle of departure (EOD) $(\theta_{tx,n,m})$ and azimuth angle of departure (AOD) $(\varphi_{tx,n,m})$
$\bar{d}_{tx,s}, \bar{d}_{rx,u}$ – the location vector of transmitting antenna element s and receiving antenna element u
$v_{n,m}$ – Doppler shift of ray n,m
$\tau_{n,m}$ – propagation delay of ray n,m

3. Results and Discussion

In this section, the dataset was used in modeling channel parameters, investigating their characteristics and reconstructing.

3.1. RMS Delay Spread Distance Dependency Model

RMS DS increases linearly with distance in the RMS DS distance dependency plot for a distance up to 200 m. The fact that the transmitted signal operates like a waveguide in a street canyon setting makes the aforementioned obvious. The RMS DS distance dependency model is given by equation (17) RMS DS and path loss have also been found to have a linear relationship as previously asserted in [42].

$$RMSDS_{StreetCanyon} = 0.4d + 25.41 \tag{17}$$

Where d (meters) is the distance between the base station and the receivers.

As illustrated in Figure 5 for the high-rise scenario, when the RMS delay spread simulation results are plotted against building height, it can be seen that the RMS DS of some groups of small cells is rather consistent over a range of height. The RMS DS, for instance, ranges from 60 to 90 nanoseconds for small cells 7 to 15 (7th to 15th floors) and from 200 to 240 nanoseconds for small cells 16 to 23 (16th to 23rd floors). These are caused by the observation of numerous clusters arriving at the same small cells at different times, with clusters 2 and 3's MPCs travelling longer paths and experiencing larger arrival delay times. Reflections from the rooftops of low-rise buildings and high-rise surroundings are the cause of the numerous arriving clusters. According to the fitted curve, the RMS DS rises as the building's height does. As a result, equation 18 provides the high-rise RMS DS distance dependence model.

$$RMSDS_{Highrise} = 0.61n^2 - 6.99n + 100 \tag{18}$$

where n is the building floor number (A floor is 3.5m height)

The authors of [25] among others investigated the RMS DS distance dependency where the generated RMS DS plot per segmented area has a linear relationship with distance Similar results would have been obtained in this study had the clusters been treated separately, but a fitted curve was utilized to connect through all clusters to demonstrate how the delay spread grows with distance for the whole building. [32, 33] and [44]are other authors that have contributed to the literature on RMS DS and distance relationships.

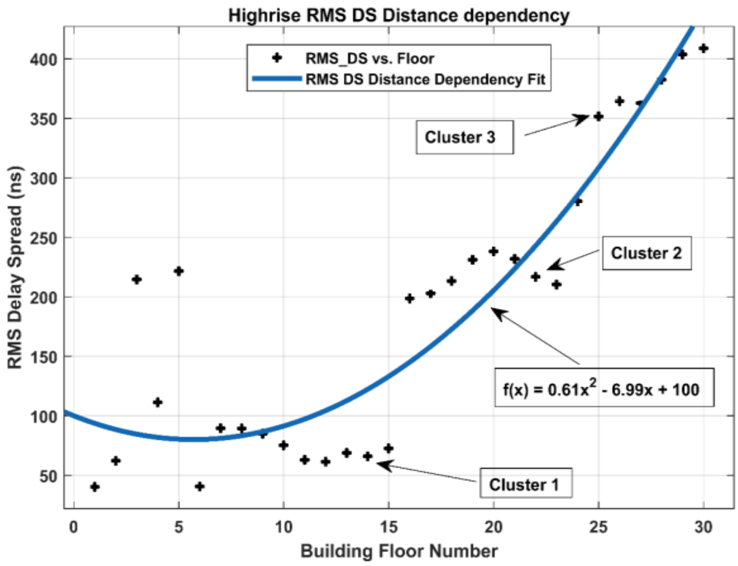

Fig. 5. RMS DS Distance Dependency Model for High-rise

3.2. RMS Delay Spread Model

A normal pdf distribution was obtained for the street canyon scenario. As seen in the distance dependency model, the RMS DS for the high-rise has three clusters due to reflections from nearby high-rise and low-rise rooftops [45] which are represented by three peaks. They are fitted by either a normal or a lognormal distribution. and are independent of one another. Rather than the carrier frequency, it has been acknowledged that DS features heavily rely on the signal bandwidth and the environment in which it propagates [46]. Using the distribution statistics, the street canyon model is displayed in equation (19).

$$f(DS)_{Street} = \frac{1}{14.44} e^{\frac{-(DS-40.98)^2}{66.36}} \tag{19}$$

The high-rise RMS DS distribution is model as follows: the distribution of the first arriving cluster is normal, but that of the second and third arriving clusters is lognormal. Their models are provided as equations (20), (21) and (22) using the statistics of the various distribution fits.

$$f(DS)_{Highrise1} = \frac{1}{51.71} e^{-\frac{(DS_{HR1} - 69.05)^2}{851.19}} \tag{20}$$

where the RMS delay spread for the first incoming cluster is the RMS DS HR_1 in equation (20).

$$f(DS)_{Highrise2} = \frac{1}{0.25 DS_{HR2}} e^{-\frac{(\log_{10} DS_{HR2} - 5.39)}{0.02}} \tag{21}$$

where RMS DS HR_2 in equation (21) is the RMS delay spread for the second arriving cluster.

$$f(DS)_{Highrise3} = \frac{1}{0.16 DS_{HR3}} e^{-\frac{(\log_{10} DS_{HR3} - 5.95)}{0.0079}} \tag{22}$$

where RMS DS HR_3 in equation (22) represents the delay spread for the third arriving cluster.

3.3. RMS Angular Spread

Angular spread depicts the spatial distribution of the incident power in addition to the angle of arrival/departure of the beams. Multipath components that arrive at a receiver from over-the-rooftop and in a high-rise propagation environment typically have a higher elevation angle spread than MPC from corridor like (wave-guided) street canyons, according to propagation measurement results [47]. To assist in assessing the possibilities of 3D MIMIO techniques like 3D beamforming and 3D sectorization, WINNER+ and the 3GPP-3D committees have been urged to incorporate elevation parameters in their models and give precise 3D channel models.

3.3.1. Street Canyon: Elevation Domain Angular Spread Distance Dependency

Regardless of the receiver's proximity to the BS, the WINNER+ standardized model assumes constant elevation dispersion for each environment. According to the findings of this work, the elevation spread for both arrival (ESA) and departure (ESD) rays decreases with distance from the BS for the street canyon scenario. The above is due to elevation ray reflections on the ground which reduces as the small cells moves away from the BS. The ESA and ESD, whose values are determined by how these angles interact, become smaller. The relationship between RMS ESA and ESD distances follows an exponential curve, with models provided by equations (23) and (24).

$$f(x)_{RMSESA} = 41.35e^{-0.15x} + 2.56e^{-0.0025x} \tag{23}$$

$$f(x)_{RMSESD} = 28.93e^{-0.108x} + 0.436e^{-0.0022x} \tag{24}$$

3.3.2. Street Canyon: Azimuth Domain Angular Spread Distance Dependency

The RMS ASA and RMS ASD values plotted against distance show a trend that the ground reflection angle theory cannot account for as both parameters move in a zigzag manner as the distance increases. The above is because ASA and ASD fluctuate in relation to changes in street structural design and physical outlay. A similar result was obtained by the authors of [25] and [48].

3.3.3. High-rise: Elevation Domain Angular Spread Distance Dependency

The RMS ESA and RMS ESD values show a linear relationship when plotted against distance, with ESA and ESD rising with building height. Equation (25) and equation (26) provide the distance dependency model for high-rise RMS ESA and RMS ESD, respectively. Other authors [39,]40] have conducted measurement-based research in a similar context where both recorded a linear relationship of ESA and ESD with height, though the author of [49] negative linearity with distance because the ESA and ESD were plotted against the BS-receiver height disparities

$$f(d)_{RMSESA} = -0.005d^2 + 0.72d - 1.37 \tag{25}$$

$$f(d)_{RMSESD} = 1.59d - 4.90 \tag{26}$$

3.3.4. High-rise: Azimuth Domain Angular Spread Distance Dependency

The RMS ASA and RMS ASD values plotted against distance reveal a negative linear connection, with ASA declining with distance and ASD rising; the RMS ASA/ASD distance dependence models are provided by equations (27) and (28).

$$f(x)_{RMSASA} = -5.46x + 36.76 \tag{27}$$

$$f(x)_{RMSASD} = 1.076x + 21.44 \tag{28}$$

3.3.5. Angular Spread Modeling: Distribution of RMS ESA and RMS ESD

The RMS ESA and RMS ESD for the high-rise and Street Canyon scenarios follows a lognormal distribution respectively. Equation (29) gives the generic model for both cases.

$$f_\theta = \frac{1}{\theta\sigma\sqrt{2\pi}} e^{\frac{-(ln\theta-\mu)^2}{2\sigma^2}} \tag{29}$$

where θ represents the elevation domain parameter, the inclusion of the distribution statistics ($\mu_{ESA,}$ μ_{ESD}, σ_{ESA}, and σ_{ESD}) for each RMS ESA or RMS ESD in the equation for the respective scenario will make the model specific to it.

3.3.6. Angular Spread Modeling: Distribution of RMS ASA and RMS ASD

The RMS ASA/ASD angular spread in the azimuth domain for the high-rise and street canyon datasets continues to have a lognormal distribution. In both cases, the generic model is given by equation (30).

$$f_\varphi = \frac{1}{\varphi\sigma\sqrt{2\pi}} e^{\frac{-(ln\varphi-\mu)^2}{2\sigma^2}} \tag{30}$$

where φ represents the azimuth domain parameter, including the distribution statistics ($\mu_{ASA,}$ μ_{ASD}, σ_{ASA}, and σ_{ASD}) for each angular spread in the equation will make the model specific. Tables 3 is the obtained angular spread statistics for high-rise and street canyon scenarios.

Table 3. Angular Spread Statistics for High-rise and Street Canyon scenarios

	High-rise		Street Canyon	
AS	μ	σ	μ	σ
RMS ASA	3.50	0.12	1.40	0.20
RMS ESA	2.45	0.20	0.60	0.16
RMS ASD	3.77	0.25	0.40	0.37
RMS ESD	3.37	0.08	0.40	0.20

3.4. 3D Channel Model of Lagos Island Reconstructed

The magnitude of the channel impulse response is plotted in figure 6 for Street Canyon LOS while other scenarios are similar with slight differences. The received waveform spectrum is plotted in figure 7 for the Street canyon LON scenario while other scenarios are similar with slight differences. Equations (31) and (32) represent the 3D model for the Street Canyon LOS and NLOS scenarios respectively, while equations (33) and (34) represent the 3D model for the High-rise LOS and NLOS scenarios respectively.

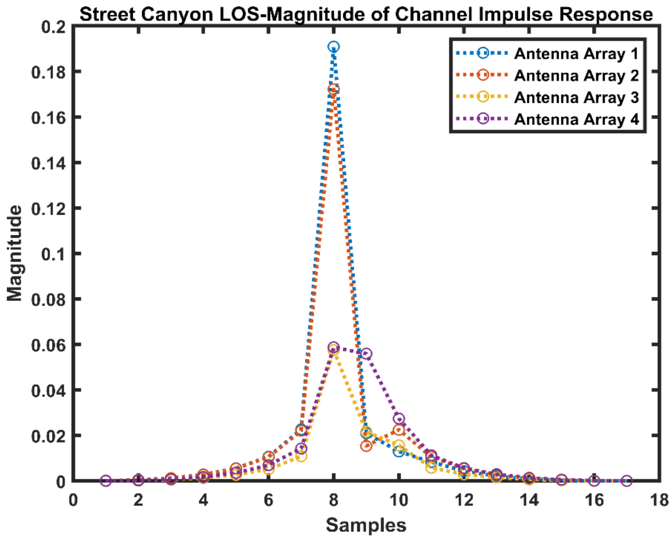

Fig. 6. Channel characteristics for Street Canyon LOS scenario

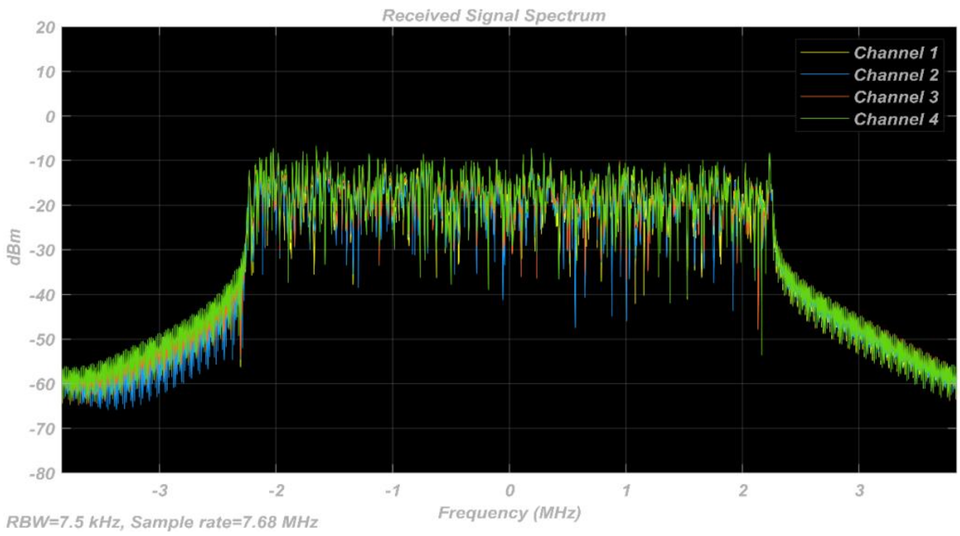

Fig. 7. Received waveform spectrum for Street Canyon LOS scenario

3.4.1. Street Canyon Line of Sight 3D model

$$H_{StreetCanyon}^{LOS}(t) = 0.3162 H_{u,s,n}^{NLOS}(t) + \delta(n-1)0.9486 \begin{bmatrix} -0.241.99 \\ 1.330.96 \end{bmatrix}^{T} \times \begin{bmatrix} e^{j\emptyset_{LOS}} & 0 \\ 0 & e^{j\emptyset_{LOS}} \end{bmatrix} \times \begin{bmatrix} -0.513.36 \\ 1.230.52 \end{bmatrix} \tag{31}$$

3.4.2. Street Canyon Non-line of Sight 3D Model

$$H_{StreetCanyon}^{NLOS}(t;\tau) = \sqrt{\frac{P_n}{M}} \sum_{m=1}^{M_n} \begin{bmatrix} -0.241.99 \\ 1.330.96 \end{bmatrix}^{T} \begin{bmatrix} e^{j\emptyset_{n,m}^{\theta\theta}} & 0.33 e^{j\emptyset_{n,m}^{\theta\varphi}} \\ 0.33 e^{j\emptyset_{n,m}^{\varphi\theta}} & e^{j\emptyset_{n,m}^{\varphi\varphi}} \end{bmatrix} \times \begin{bmatrix} -0.513.36 \\ 1.230.52 \end{bmatrix} \tag{32}$$

3.4.3. High-rise Line of Sight 3D Model

$$H_{UrbanHighRise}^{LOS}(t) = 0.58 H_{u,s,n}^{NLOS}(t) + \delta(n-1)0.82 \begin{bmatrix} 2.453.50 \\ 0.200.12 \end{bmatrix}^{T} \times \begin{bmatrix} e^{j\emptyset_{LOS}} & 0 \\ 0 & e^{j\emptyset_{LOS}} \end{bmatrix} \times \begin{bmatrix} 3.273.77 \\ 0.220.25 \end{bmatrix} \tag{33}$$

3.4.4. High-rise Non-line of Sight 3D Model

$$H_{UrbanHighRise}^{NLOS}(t;\tau) = \sqrt{\frac{P_n}{M}} \sum_{m=1}^{M_n} \begin{bmatrix} 2.453.50 \\ 0.200.12 \end{bmatrix}^{T} \begin{bmatrix} e^{j\emptyset_{n,m}^{\theta\theta}} & 0.707 e^{j\emptyset_{n,m}^{\theta\varphi}} \\ 0.707 e^{j\emptyset_{n,m}^{\varphi\theta}} & e^{j\emptyset_{n,m}^{\varphi\varphi}} \end{bmatrix} \times \begin{bmatrix} 3.273.77 \\ 0.220.25 \end{bmatrix} \tag{34}$$

4. Conclusion

A ray tracing-based mmWave channel investigation has been conducted in a metropolitan city for cellular canyon and high-rise propagation scenarios. The rms delay spread, rms azimuth spread of arrival, rms elevation spread of arrival, elevation domain angular spread, azimuth domain angular spread were investigated relative to the canyon and high rise setting and relevant models were postulated. A consequent 3D channel state information was reconstructed following an algorithmic outline based on the findings in this work. The results provide an opportunity to adapt the transmitted signal to the CSI and thereby optimize the received signal for spatial multiplexing or to achieve low bit error rates in wireless communication.

Acknowledgements

This work was supported by the REMCOM Corporation State College, PA 16801 USA.

References

[1] Q. Nadeem, S. Member, and A. Kammoun, “Elevation Beamforming with Full Dimension MIMO Architectures in 5G Systems : A Tutorial,” pp. 1–31.

[2] Y. Li, X. Ji, D. Liang, and Y. Li, “Dynamic Beamforming for Three-Dimensional MIMO Technique in LTE-Advanced Networks,” vol. 2013, 2013.

[3] D. C. Araújo, T. Maksymyuk, A. L. F. de Almeida, T. Maciel, J. C. M. Mota, and M. Jo, “Massive MIMO: Survey and future research topics,” *IET Commun.*, vol. 10, no. 15, pp. 1938–1946, 2016, doi: 10.1049/iet-com.2015.1091.

[4] S. Chen, T. Zhao, H. H. Chen, and W. Meng, “Network Densification and Path-Loss Models Versus UDN Performance - A Unified Approach,” *IEEE Trans. Wirel. Commun.*, vol. 20, no. 7, pp. 4058–4071, 2021, doi: 10.1109/TWC.2021.3055549.

[5] R. Q. Shaddad, A. A. Saeed, R. Q. Naji, and A. M. Baalawi, “Hybrid Traffic Dispersion and Network Densification Scheme for 5G Millimeterwave Wireless Networks,” *2019 1st Int. Conf. Intell. Comput. Eng. Towar. Intell. Solut. Dev. Empower. our Soc. ICOICE 2019*, pp. 1–6, 2019, doi: 10.1109/ICOICE48418.2019.9035153.

[6] O. Idowu-bismark and F. Idachaba, “5G Small Cell Backhaul : A Solution Based on GSM-Aided Hybrid Beamforming,” no. August, pp. 24–31, 2019, doi: 10.5815/ijcnis.2019.08.03.

[7] H. Ji, Y. Kim, J. Lee, and S. Electronics, “Overview of Full-Dimension MIMO in LTE-Advanced Pro Overview of Full-Dimension MIMO in LTE-Advanced Pro”.

[8] Q. Nadeem, S. Member, and A. Kammoun, “3D Massive MIMO Systems : Modeling and Performance Analysis,” vol. 14, no. 12, pp. 6926–6939, 2015.

[9] Y. Han, T. Hsu, C. Wen, K. Wong, and S. Jin, “Efficient Downlink Channel Reconstruction for FDD Multi-Antenna Systems,” pp. 1–23.

[10] G. Xu *et al.*, “Full Dimension MIMO (FD-MIMO): Demonstrating Commercial Feasibility,” *IEEE J. Sel. Areas Commun.*, vol. 35, no. 8, 2017, doi: 10.1109/JSAC.2017.2711150.

[11] M. Ozates, M. Kazemi, and T. M. Duman, “Channel Reconstruction Based Multiuser Precoding with Limited Feedback,” pp. 0–5, 2021, doi: 10.1109/BlackSeaCom52164.2021.9527824.

[12] C. Chang and D. W. Lin, “Interpolative Reconstruction of Millimeter Wave Mobile Channel Responses from Randomly Scattered Snapshots,” 2017.

[13] Q. Zhu *et al.*, “Effects of Digital Map on the RT-based Channel Model for UAV mmWave Communications”.

[14] J. Kaleva, N. J. Myers, T. Antti, R. W. H. Jr, and U. Madhow, “Short Range 3D MIMO mmWave Channel Reconstruction via Geometry-aided AoA Estimation,” pp. 427–431, 2019.

[15] N. Prasad and X. F. Qi, “Channel Reconstruction in Intelligent Surface aided Communications,” vol. 2061, pp. 531–539.

[16] W. Ma *et al.*, "Sparse Channel Estimation and Hybrid Precoding Using Deep Learning for Millimeter Wave Massive MIMO," vol. 68, no. 5, pp. 2838–2849, 2020.
[17] O. B. Idowu-Bismark, A. E. Ibhaze, and A. A. Atayero, "Mimo Optimization Techniques and Their Application in Maximizing Throughput for 3GPP HSPA+," *J. Wirel. Netw. Commun.*, vol. 7, no. 1, pp. 1–8, 2017, doi: 10.5923/j.jwnc.20170701.01.
[18] S. A. Busari, K. M. S. Huq, S. Mumtaz, L. Dai, and J. Rodriguez, "Millimeter-Wave Massive MIMO Communication for Future Wireless Systems: A Survey," *IEEE Commun. Surv. Tutorials*, vol. 20, no. 2, pp. 836–869, 2018, doi: 10.1109/COMST.2017.2787460.
[19] F. Boccardi, R. W. Heath, T. Marzetta, and P. Popovski, "Five Disruptive Technology Directions for 5G," no. December 2013, 2014, doi: 10.1109/MCOM.2014.6736746.
[20] R. A. F. S. Perspective *et al.*, "Accuracy Versus Complexity for mmWave," *IEEE Trans. Wirel. Commun.*, vol. 20, no. 12, pp. 7826–7841, 2021, doi: 10.1109/TWC.2021.3088349.
[21] O. Idowu-Bismark, O. Kennedy, R. Husbands, and M. Adedokun, "5G wireless communication network architecture and its key enabling technologies," *Int. Rev. Aerosp. Eng.*, vol. 12, no. 2, 2019, doi: 10.15866/irease.v12i2.15461.
[22] T. A. Thomas and H. C. Nguyen, "3D mmWave Channel Model Proposal," 2014.
[23] Y. Zhang, J. Zhang, J. Zhang, G. Liu, Y. Zhang, and Y. Yao, "A Theoretical Analysis of Favorable Propagation on Massive MIMO Channels with Generalized Angle Distributions," *Electronics*, vol. 11, no. 14, p. 2150, 2022, doi: 10.3390/electronics11142150.
[24] A. Tkac and V. Wieser, "Channel Estimation Using Measurement of Channel Impulse Response," no. May, 2014, doi: 10.1109/ELEKTRO.2014.6847883.
[25] R. Zhang, X. Lu, J. Zhao, L. Cai, and J. Wang, "Measurement and modeling of angular spreads of three-dimensional urban street radio channels," *IEEE Trans. Veh. Technol.*, vol. 66, no. 5, pp. 3555–3570, 2017, doi: 10.1109/TVT.2016.2604394.
[26] L. Tian, J. Zhang, H. Tan, P. Tang, and G. Liu, "Propagation characteristics of elevation angles and three dimensional fading channel model with angle offset," *China Commun.*, vol. 16, no. 9, pp. 62–78, 2019, doi: 10.23919/JCC.2019.09.005.
[27] ITU-R, "M.2135 Guidelines for evaluation of radio interface technologies for IMT-Advanced," vol. 1, 2009.
[28] Q. U. A. Nadeem, A. Kammoun, and M. S. Alouini, "Elevation Beamforming with Full Dimension MIMO Architectures in 5G Systems: A Tutorial," *IEEE Commun. Surv. Tutorials*, vol. 21, no. 4, pp. 3238–3273, 2019, doi: 10.1109/COMST.2019.2930621.
[29] C. Seker, M. T. Guneser, and H. Arslan, "Millimeter-wave propagation modeling and characterization at 32 GHz in indoor office for 5G networks," *Int. J. RF Microw. Comput. Eng.*, vol. 30, no. 12, pp. 1–12, 2020, doi: 10.1002/mmce.22455.
[30] M. Kyrö, V. M. Kolmonen, and P. Vainikainen, "Experimental propagation channel characterization of mm-wave radio links in urban scenarios," *IEEE Antennas Wirel. Propag. Lett.*, vol. 11, pp. 865–868, 2012, doi: 10.1109/LAWP.2012.2210532.
[31] S. G. Larew, T. a Thomas, M. Cudak, and A. Ghosh, "Air interface design and ray tracing study for 5G millimeter wave communications," *2013 IEEE Globecom Work. (GC Wkshps)*, pp. 117–122, 2013, doi: 10.1109/GLOCOMW.2013.6824972.
[32] G. R. Maccartney, T. S. Rappaport, M. K. Samimi, and S. Sun, "Millimeter-Wave Omnidirectional Path Loss Data for Small Cell 5G Channel Modeling," *IEEE Access*, vol. 3, pp. 1573–1580, 2015, doi: 10.1109/ACCESS.2015.2465848.
[33] S. Hur *et al.*, "Proposal on millimeter-wave channel modeling for 5G cellular system," *IEEE J. Sel. Top. Signal Process.*, vol. 10, no. 3, pp. 454–469, 2016, doi: 10.1109/JSTSP.2016.2527364.
[34] S. Ju, Y. Xing, O. Kanhere, and T. S. Rappaport, "Millimeter Wave and Sub-Terahertz Spatial Statistical Channel Model for an Indoor Office Building," *IEEE J. Sel. Areas Commun.*, vol. 39, no. 6, pp. 1561–1575, 2021, doi: 10.1109/JSAC.2021.3071844.
[35] S. K. Hinga and A. A. Atayero, "Deterministic 5G mmWave Large-Scale 3D Path Loss Model for Lagos Island, Nigeria," *IEEE Access*, vol. 9, pp. 134270–134288, 2021, doi: 10.1109/ACCESS.2021.3114771.
[36] S. Zhdanov, N. Kadet, V. Silkov, M. Zirka, O. Rasstrygin, and A. Zirka, "The mathematical model for research of the UAV longitudinal moving," *Int. J. Comput. Netw. Inf. Secur.*, vol. 13, no. 5, pp. 29–39, 2021, doi: 10.5815/ijcnis.2021.05.03.
[37] H. Lee *et al.*, "Downlink Channel Reconstruction for Spatial Multiplexing in Massive MIMO Systems," pp. 1–12.
[38] Q. Gao, Z. Li, W. Zhang, X. Bao, J. Xia, and Z. Zheng, "Channel reconstruction for mmWave Massive MIMO systems based on Channel Path Map," *Phys. Commun.*, vol. 61, p. 102232, Dec. 2023, doi: 10.1016/J.PHYCOM.2023.102232.
[39] W. Fan, F. Zhang, Z. Wang, O. K. Jensen, and G. F. Pedersen, "On Angular Sampling Intervals for Reconstructing Wideband Channel Spatial Profiles in Directional Scanning Measurements," vol. 9545, no. c, pp. 1–6, 2020, doi: 10.1109/TVT.2020.3030029.
[40] T. Specification, G. Radio, and A. Network, "3gpp tr 36.873," vol. 0, no. Release 12, 2014.
[41] S. K. Hinga and A. A. Atayero, "Deterministic 5G mmWave Large-Scale," *IEEE Access*, vol. PP, p. 1, 2021, doi: 10.1109/ACCESS.2021.3114771.
[42] T. S. Rappaport *et al.*, "Millimeter wave mobile communications for 5G cellular: It will work!," *IEEE Access*, vol. 1, pp. 335–349, 2013, doi: 10.1109/ACCESS.2013.2260813.
[43] Z. Yasser, "RMS Delay Spread and Path Loss Dependency for Mobile Outdoor UWB Channels," *2018 Int. Conf. Adv. Sci. Eng.*, pp. 206–211, 2018.
[44] O. Idowu-Bismark, F. Idachaba, A. A. Atayero, W. Janusz, and C. Harling, "RMS Delay Spread and Channel Capacity Modelling for 28 GHz MIMO Channel with Different UE Height," *Lect. Notes Networks Syst.*, vol. 286, pp. 663–671, 2022, doi: 10.1007/978-981-16-4016-2_63.
[45] X. Y. Wang, B. Li, X. Yuan, J. W. Dou, and Y. Li, "Elevation angle research in three-dimension channel model using ray-tracing," *2014 31th URSI Gen. Assem. Sci. Symp. URSI GASS 2014*, no. i, pp. 3–6, 2014, doi: 10.1109/URSIGASS.2014.6929281.
[46] P. F. M. Smulders and L. M. Correia, "Characterisation of propagation in 60 GHz radio channels," *Electron. Commun. Eng. J.*, vol. 9, no. 2, pp. 73–80, 1997, doi: 10.1049/ecej:19970204.
[47] R. N. Almesaeed, A. S. Ameen, E. Mellios, A. Doufexi, and A. Nix, "3D channel models: Principles, characteristics, and system implications," *IEEE Commun. Mag.*, vol. 55, no. 4, pp. 152–159, 2017, doi: 10.1109/MCOM.2017.1500505.
[48] O. Idowu-Bismark, F. Idachaba, and A. A. Atayero, "Large-scale parameter modelling for millimeter-wave multiple-input multiple-output channel in 5G ultra-dense network," *Indones. J. Electr. Eng. Comput. Sci.*, vol. 26, no. 2, pp. 794–807, 2022, doi: 10.11591/ijeecs.v26.i2.pp794-807.

[49] "R1-132988 Proposals for 3D MIMO Channel Modelling in UMi_final."
[50] R. Zhang, X. Lu, W. Duan, L. Cai, and J. Wang, "Elevation domain channel measurement and modeling for FD-MIMO with different UE height," *2015 IEEE Wirel. Commun. Netw. Conf. WCNC 2015*, no. Wcnc, pp. 70–75, 2015, doi: 10.1109/WCNC.2015.7127447.

Authors' Profiles

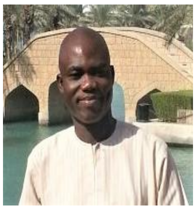

Olabode Idowu-Bismark is a Senior Lecturer at Covenant University, Ota, Nigeria. He holds a B.Eng. degree in Electrical and Electronics Engineering from the University of Benin, Nigeria, and a M.Sc. in Telecommunications Engineering from Birmingham University, UK. He obtained his Ph.D. in Information and Communication Engineering from Covenant University. He is also a Faculty Member of the Covenant Applied Informatics and Communication Africa Centre of Excellence (CApIC-ACE), a World Bank ACE-IMPACT Centre, Covenant University. Olabode has worked in various companies as an engineer, senior engineer, and technical manager. He is a member of the Nigerian Society of Engineers, a member of MIEEE, and a COREN Registered Engineer. His research interest is in the area of mobile communication, mmWave, and MIMO communication. He has published many scientific papers in international peer-reviewed journals and conferences.

Oluwadamilola Oshin received the Ph.D. degree in information and communication engineering (with a focus on nano-electronic biosensing) from Covenant University, Nigeria, in 2020. She is a Senior Lecturer of information and communication engineering with the Department of Electrical and Information Engineering, Covenant University. She is also a Faculty Member of the Covenant Applied Informatics and Communication Africa Centre of Excellence (CApIC-ACE), a World Bank ACE-IMPACT Centre, Covenant University. She has broad research experiences and interests including mobile communications, data analytics, artificial intelligence, and MEMS-based biosensing. She is professionally registered with the Council for the Regulation of Engineering in Nigeria (COREN) and is also a member of the Institute of Electrical and Electronics Engineers (IEEE). She enjoys teaching, research and solving health-related issues using engineering and technology.

Prof. Emmanuel Adetiba a member of IEEE, received the Ph.D. degree in information and communication engineering from Covenant University, Ota, Nigeria. He was the Director of the Center for Systems and Information Services (aka ICT Center), Covenant University, from 2017 to 2019. He is the incumbent Deputy Director of the Covenant Applied Informatics and Communication Africa Centre of Excellence (CApIC-ACE) and a Co-PI of the FEDGEN Cloud Computing Research Project at the center (World Bank and AFD funded). He is the Founder and a Principal Investigator of the Advanced Signal Processing and Machine Intelligence Research (ASPMIR) Group. He is a Full Professor and the former Head of the Department of Electrical and Information Engineering, Covenant University, from 2021 to 2023. He is also a member of the HRA, Industrial Engineering Department, Durban University of Technology, Durban, South Africa. His research interests and experiences include machine intelligence, software-defined radio, cognitive radio, biomedical signal processing, and cloud and high-performance computing (C&HPC). He is a registered engineer (R. Engr) with the Council for the Regulation of Engineering in Nigeria (COREN) and a member of the Institute of Information Technology Professionals (IITP), South Africa.

How to cite this paper: Olabode Idowu-Bismark, Oluwadamilola Oshin, Emmanuel Adetiba, "3D mmWave MIMO Channel Modeling and Reconstruction for Street Canyon and High-rise Scenarios", International Journal of Wireless and Microwave Technologies(IJWMT), Vol.15, No.3, pp. 19-36, 2025. DOI:10.5815/ijwmt.2025.03.02